ACS Catalysis

Research Article

pubs.acs.org/acscatalysis

Shape-Dependent Activity of Ceria in Soot Combustion

Eleonora Aneggi,[†] Dawid Wiater,[†] Carla de Leitenburg,[†] Jordi Llorca,[‡] and Alessandro Trovarelli*,[†]

[†]Dipartimento di Chimica, Fisica e Ambiente, Università di Udine, 33100 Udine, Italy

[‡]Institut de Tècniques Energètiques, Universitat Politècnica de Catalunya, 08028 Barcelona, Spain

ABSTRACT: In this study, a series of conventional polycrystalline ceria and single-crystalline ceria nanorods and nanocubes were prepared by hydrothermal methods, and their structural, redox, and morphological properties were investigated using XRD, SEM, HRTEM, BET, temperature-programmed reduction, and oxygen storage capacity measurements. According to HRTEM, they are characterized by exposure of different surfaces: {100} surface for nanocubes; {100}, {110}, and in part {111} for nanorods; and mainly {111} for conventional polycrystalline ceria, with a morphology dominated by {111}-enclosed octahedral particles. The presence of more-reactive exposed surfaces affects the reaction of soot oxidation positively, with an increase in activity in nanoshaped materials compared with conventional ceria. Thermal aging, although detrimental for surface area, is shown to affect morphology by promoting irregular truncation of edges and corners and development of more reactive surface combinations in all crystal shapes. It is likely that thermal treatment, starting from either cubes or octahedral particles, induces the formation of a similar particle geometry whose activity is dependent on the type of plane exposed and by the number an extension of edge and corners, thus linking reactivity of octahedral particles in conventional ceria powders with that of cubes in nanoshaped materials. The results indicate that soot oxidation is also a surface-dependent reaction, and catalyst design for this purpose should allow for surface structure morphology and its evolution against temperature.

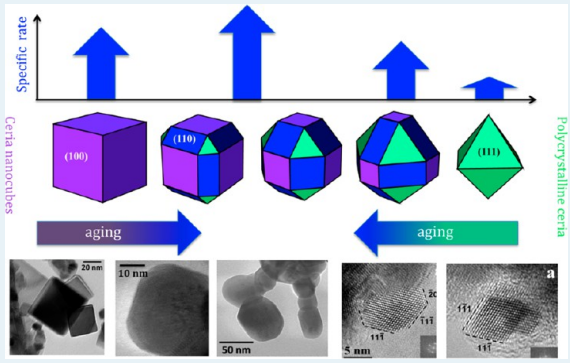

KEYWORDS: *ceria, soot oxidation, nanocubes, nanorods, combustion, CeO_2*

1. INTRODUCTION

During recent years, the preparation of nanoparticles (NPs) with controlled shapes and morphologies has shown a rapid increase, and great attention has been paid to the use of these materials in catalysis and related fields.[1,2] From these studies, it is now clear that the properties of nanomaterials are affected not only by crystal size but also by crystal shape and, therefore, by the nature of the exposed facets and by the type and disposition of atoms present on the surface.

Ceria is a key component of catalyst formulations for several applications in the environment and energy sector,[3] and these applications benefit from ceria redox properties, which are in turn associated with the arrangement of its surfaces and the shape and dimensions of its crystals. The shape of conventional polycrystalline ceria is dominated by {111}-enclosed octahedral with flat surfaces, whereas for smaller particles, truncated octahedral shape may be found.[4] The role of shape dependency on catalytic activity was first tested on CeO_2.[5] This study showed that although surface area of nanoshaped ceria was lower than that of polycrystalline materials, they exhibit higher catalytic activity in CO oxidation. This was correlated to the exposure of reactive crystal planes in CeO_2 nanoparticles: ceria nanorods with well-defined reactive planes {001} and {110} are more active than conventional ceria NPs with preferred exposure of {111} planes. Successively, the facet-dependent activity of CO oxidation in ceria has been confirmed for other nanostructures[6−10] and the same positive effect has been reported for other reactions, such as CO_2 reforming of methane,[11] methanol and ethanol reforming,[12,13] and low-temperature water-gas shift.[14−16]

The higher activity of specific ceria surfaces was also found in ceria films grown with different orientations.[17] A shape-selective synthetic approach resulted also in the preparation of ceria nanostructures with a higher oxygen storage capacity (OSC) due to exposure of more reactive planes, which allowed oxygen storage to take place both at the surface and in the bulk.[18,19] Cubic nanoceria was also reported to offer high OSC at temperatures as low as 150 °C.[20] The majority of these results, which rely on the redox properties of ceria and its ability to release/capture oxygen, are supported by theoretical evidence that correlate higher activity to the lower stability of {100} and {110}-type surfaces compared with {111} and to their lower energy of oxygen vacancies formation.[21,22]

The ability of ceria to promote oxygen storage/redox behavior is also at the basis of its application as a catalyst for combustion of soot particulate under conditions typical of diesel car exhaust.[23,24] The use of CeO_2 and CeO_2-based materials has received increased attention in the past decade as a result of the extremely good soot oxidation temperatures displayed by ceria and related materials,[25−31] which is

Received: September 24, 2013
Revised: December 4, 2013
Published: December 5, 2013

associated with the availability of surface active oxygens coupled with surface reducibility. It is clear from previous investigations that to improve efficiently the soot oxidation abilities of ceria, it is important to modify its redox capacity and to implement the formation of active oxygen species. Therefore, any processing conditions that result in preferential exposure or redox-reactive surfaces is expected to enhance reactivity toward soot particle oxidation.

In our previous studies, we showed that the thermal treatment of polycrystalline ceria promotes structural evolution, causing the exposure of more reactive surfaces (i.e., {100} and {110} facets), whereas exposure of {111} faces progressively reduces exposure. This resulted in a remarkable increase in the specific reaction rate for oxidation of CO.[32] More recently, the same effect was observed in the oxidation of soot;[33] however, in both cases, the exposure of more reactive surfaces was obtained following an aging treatment at the expense of the surface area, and although the specific reaction rate increased, the overall activity (on a per gram basis) did not show any benefit. It is obvious that the catalytic activity of CeO_2 in soot oxidation depends also on its specific surface area,[30] and therefore, it is important to promote the quality of catalytic sites by exposure of reactive surfaces without losing the quantity of available surface sites. For these reasons, we have prepared a series of nanoshaped cerias with cubic and rod shapes and compared for the first time their activity in soot oxidation (both specific rate and overall activity) with the activity of irregularly shaped polycrystalline ceria. This allowed us to overcome the limitation of previous studies by successfully preparing a series of shape-controlled materials with higher activity in soot oxidation, as compared with polycrystalline ceria.

2. EXPERIMENTAL SECTION

2.1. Materials. Two types of shape-controlled nanocerias (nanocubes and nanorods) were prepared according to previously reported methodologies.[34−36] For ceria nanocubes (CeO_2-NC) a NaOH solution (57.60 g of NaOH dissolved in 210 mL of distilled water) was added dropwise into a $Ce(NO_3)_3{\cdot}6H_2O$ solution (5.21g of $Ce(NO_3)_3{\cdot}6H2O$ in 30 mL of distilled water) under vigorous mixing. After precipitation, the suspension was transferred to a Teflon-lined cylinder and sealed tightly in a stainless steel autoclave. The suspension was heated for 24 h at 453 K; after cooling, the mixture was centrifuged and washed three times in water and then in ethanol for separation and purification of the powder. Finally, the powder was dried at 333 K overnight to obtain the starting material. Samples for catalytic purposes were aged under air atmosphere at 723 K (fresh samples) and 1023 K (aged samples) for 4 h. Ceria nanorods (CeO_2-NR) were obtained by adding dropwise a NaOH solution (75.59 g of NaOH dissolved in 200 mL of distilled water) into a solution of $CeCl_3{\cdot}7H_2O$ (5.36 g in 40 mL of distilled water). After precipitation and transfer to the autoclave, the mixture was heated at 410 K for 48 h, followed by cooling, separation, washing, and drying to obtain the starting material. Calcination of the sample at 723 or 1023 K was carried out before use in soot oxidation. The preparations were repeated several times to check for reproducibility and to obtain the desired quantities.

Polycrystalline conventional ceria sample (CeO_2-CV) was prepared according to a process that involves the precipitation of a homogeneous acidic solution of cerium nitrate with a base. The filter cake was then washed with distilled water, followed by drying and calcination at 773 K (starting sample). The material was further treated at 973 and 1073 K for 2 h to obtain a powder having a surface area comparable to that of fresh and aged nanoshaped materials. In summary, for each class of materials, we obtained two samples (fresh and aged) characterized by similar values of surface areas (in the range 27−42 m^2/g for fresh cerias and 9−14 m^2/g for aged samples). In the case of conventional ceria, the starting sample characterized by a surface area of 93 m^2/g was also used for comparison purposes.

2.2. Characterization of Materials. Textural characteristics of powders were measured according to the BET method by nitrogen adsorption at 77 K using a Tristar 3000 gas adsorption analyzer (Micromeritics).

Structural features of the catalysts were investigated by X-ray diffraction. Diffractograms were recorded on a Philips X'Pert diffractometer (equipped with a real time multiple strip detector) operated at 40 kV and 40 mA using Ni-filtered Cu Kα radiation. X-ray profiles were collected using a step size of 0.02° and a counting time of 40s per angular abscissa in the range 20−90°. The Philips X'Pert HighScore software was used for phase identification. The mean crystalline size was estimated from the full width at the half-maximum (fwhm) of the main diffraction peak using the Scherrer equation[37] with a correction for instrument line-broadening. Rietveld refinement of X-ray diffraction (XRD) spectra was performed by means of GSAS-EXPGUI program.[38,39]

For high-resolution transmission electron microscopy studies (HRTEM), a JEOL JEM 2010F electron microscope equipped with a field emission gun working at an accelerating voltage of 200 kV was used. Samples were dispersed in ethanol in an ultrasonic bath, and a drop of supernatant suspension was poured onto a holey carbon-coated grid and dried completely before measurements. Samples have been characterized also by FESEM using a Neon40 Crossbeam Station (Zeiss) instrument with low electron beam energy (5 kV). The samples have been mounted on flat Si substrates from suspensions under ultrasounds and sputtered with C to avoid charging effects.

Reduction behavior was measured by temperature-programmed reduction experiments (TPR) with an AutoChem II 2920 instrument (Micromeritics). After a pretreatment under air at 723 K for 1 h, samples (50−60 mg) were heated from room temperature to 1073 K at a constant rate (10 K/min) in a U-shaped quartz reactor under a flowing hydrogen/argon mixture (35 mL/min, 5% H_2 in Ar) while monitoring the hydrogen consumption with a TCD detector calibrated with the reduction of known amounts of CuO.

Oxygen storage capacity (OSC) of samples was investigated by carrying out TGA experiments in Ar/(5%)H_2 mixture flow (100 mL/min). Each sample was treated in an Ar atmosphere for 1 h at 553 K, followed by heating at a constant rate (10 K/min) up to 673 K and kept at this temperature for 15 min to eliminate the adsorbed water. Finally, an Ar/H_2 mixture was introduced while keeping the temperature at 673 K for 30 min. The observed weight loss is due to oxygen removal by H_2 to form water, and it can be associated with total oxygen storage capacity at that temperature.[30,40]

2.3. Catalytic Activity. Soot oxidation activity was measured under O_2/N_2 mixtures by running TGA experiments (Q500, TA Instruments) and measuring the weight loss against temperature of catalyst/soot mixtures under flowing air. Approximately 20 mg of sample (soot mixed with catalyst) was placed in a small, flat Pt crucible licked by an air flow (60 mL/min) tangent to the sample. This mixture was pretreated

dx.doi.org/10.1021/cs400850r | ACS Catal. 2014, 4, 172−181

for 1h at 423 K to eliminate traces of adsorbed water, then it was heated at a constant rate (10 K/min) up to 1073 K. As a measure of activity, we used the temperature at which 50% of weight loss is observed (T_{50}, corresponding to the temperature at which 50% of soot is converted under working conditions). Reproducibility of results was tested by running several TG experiments on similar samples, and the results in terms of T_{50} were always within ±5 K.

For the preparation of the mixture between soot and catalyst, both tight and loose contact were used. Each catalyst was accurately mixed with soot (Printex-U, Degussa AG, soot/catalyst ratio 1/20) in a mortar for 10 min to achieve a tight contact or for 2 min with a spatula for the loose contact conditions.

To study the effect of lattice oxygen of ceria, soot oxidation activity experiments in the absence of gas phase oxygen were also carried out. The experiments consisted of a temperature-programmed reduction under inert gas flow using known amounts of catalysts mixed with soot, which acts as reductant. Samples were pretreated for 1 h at 423 K to eliminate adsorbed water, and then they were heated under inert atmosphere (N_2@100 mL/min) at a constant rate (10 K/min) up to 1073 K. The weight loss of the sample is due to formation of CO/CO_2 mixtures and is a measure of the activity of soot oxidation by oxygen from the catalyst. As an indication of activity, we used the weight loss in the range from 423 to 1073 K.

Reaction rate measurements were performed by isothermal experiments at 673 and 773 K. Approximately 20 mg of a catalyst-soot mixture (soot/catalyst weight ratio 1/20) was pretreated for 1 h at 423 K under nitrogen atmosphere, then it was heated at a constant rate (10 K/min) up to the reaction temperature, followed by switching to air. The reaction was followed for 1 h using the weight loss rate as a measure of the soot oxidation rate. The specific reaction rate was determined according to Van Setten et al.[41] and normalized to the soot initially present in the reactor and to the catalyst surface area ($\mu g_{soot} \cdot g_{soot\_initial} \cdot s^{-1} \cdot m^{-2}$). The specific reaction rate was calculated for different degrees of soot conversion (5−50%), and for the sake of clarity, we will use in this study the results obtained for 5% conversion. Similar conclusions can be reached using higher conversion values. Apparent activation energies for reaction under tight contact conditions were calculated from reaction rate measurements in the temperature range 623−723 K.

3. RESULTS

3.1. Structural and Morphological Characterization of Materials. The crystalline structure of ceria nanopowders was investigated by XRD. The diffraction profiles for the three class of materials are reported in Figure 1; the main reflections can be indexed to (111), (200), (220), (311), (222), (400), (331), and (420) planes according to a pure fluorite cubic structure (space group *Fm*3*m*, JCPDS 01-075-0120). Calculated lattice parameters are in line with that reported for bulk ceria (0.54110 nm) for conventional samples, whereas for CeO_2 nanorods and nanoscubes, they are slightly lower (Table 1). A more significant variation of the lattice parameter of ceria has been already reported and associated with grain surface relaxation of small nanoparticles.[42] Interestingly, the intensity of the diffraction peaks changed with the morphology of the CeO_2 nanocrystals. Compared with the reference, the intensity ratio between reflections corresponding to (200), (220), (311), (400), (331), (420) planes and (111) and (222) is increased in

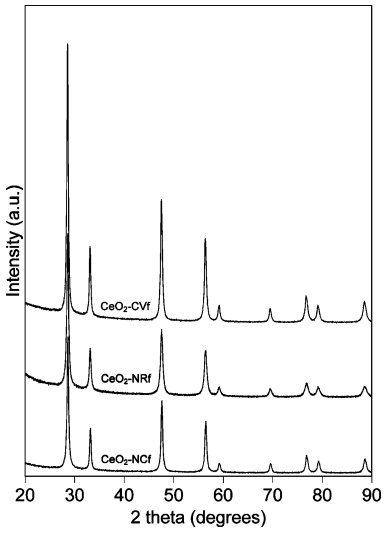

Figure 1. XRD profiles of fresh polycrystalline ceria, ceria nanocubes and ceria nanorods.

cubes, but for rods, the intensity ratio between (200) and (220) drops from a value of ∼0.6 for the reference material to a value of ∼0.52, a decrease that is reported to reflect the direction of the lattice parameter growing axis; in this case, [220][6,43,44] (Table 1). Table 1 also shows particle size (as determined from the Scherrer equation[37]) and surface area data that agree with values reported in the literature; a significant drop in the surface area is observed following aging at 1023 K. Conventional ceria powders after calcination at 973 and 1073 K show surface area values comparable to those found in nanoshaped cerias.

FESEM and HRTEM analyses were carried out on all nanomaterials to fully characterize their average size and shape. Figure 2 shows micrographs of ceria nanocubes and nanorods in the starting state. Nanocube samples consist of very homogeneous particles (Figure 2a), and their cubic morphology is clearly seen at higher magnification (Figure 2b). It is interesting to note that there are particles with different sizes, but they always exhibit cube morphology. The edges of the cubes range from 20 to 200 nm; most of them are ∼50 nm. There is only a minor part of the sample that had a nondefined morphology, but in any case, we can conclude that more than 95% of the sample consists of nanocubes. The calcination treatment at 723 K does not result in any appreciable change in morphology compared with starting materials, in agreement with previous investigations that show morphological modifications starting above 773 K.[36] Nanorods (Figure 2c,d) show an average width of about 40−50 nm with a length varying in the range of a few hundred nanometers. Also in this case, calcination at 723 K does not result in any appreciable change in morphology.

HRTEM images of fresh nanocubes and nanorods are collected in Figure 3. Figure 3a,b corresponds to lattice fringe images of ceria nanocubes. As stated above, the sample consists of nanocubes of different sizes. The (200) crystallographic planes of CeO_2 are easily distinguished in those nanocubes oriented along the [100] direction (spots at 2.71 Å in the Fourier transform images), as in Figure 3b. Figure 3c,d corresponds to HRTEM images of ceria nanorods. In this case, several CeO_2 planes are recognized, in agreement with the nanorod morphology, as previously described.[15,35] Figure 3d shows a domain oriented along the [111] crystallographic

dx.doi.org/10.1021/cs400850r | ACS Catal. 2014, 4, 172−181

Table 1. Structural, Textural, and Reduction Properties of Investigated Samples

	CeO_2-CV	CeO_2-CV_f	CeO_2-CV_a	CeO_2-NC_f	CeO_2-NC_a	CeO_2-NR_f	CeO_2-NR_a
aging T (K), time (h)	773 (2)	973 (2)	1073 (2)	723 (2)	1023 (2)	723 (2)	1023 (2)
lattice parameter (nm)	0.54110	0.54109	0.54107	0.54060	0.54082	0.54097	0.54073
particle size (nm)	17	51	92	46	86	44	55
surface area (m^2/g)	93	42	13	27	14	33	9
reduction[a] (x in CeO_x)	1.82	1.83	1.82	1.77	1.75	1.79	1.78
OSC (μmoles O/m^2)	0.8	0.4	0.9	6.8	11.2	6.3	9.9
OSC_{calc}[b] (μmoles O/m^2)	6.6	6.6	6.6	5.7	5.7	4.9	4.9
planes	ref[c]	CeO_2-CV_f	CeO_2-CV_a	CeO_2-NC_f	CeO_2-NC_a	CeO_2-NR_f	CeO_2-NR_a
111	100	100	100	100	100	100	100
200	27	27	29	32	31	25	26
220	45	42	45	56	53	47	47
311	33	31	30	41	39	33	33
222	6	5	5	7	7	6	5
400	5	5	5	7	7	6	5
331	10	9	10	14	13	11	9
420	6	6	7	9	8	7	6

[a]Value of x in CeO_x as measured at the end of a TPR run from hydrogen consumption. [b]Calculated according to the theoretical OSC of (100), (110), and (111) surfaces for CeO_2 in the literature, which are 5.7, 4.0, and 6.6 μmol O/m^2, respectively. [c]Reference value from JCPDS 01-075-0120.

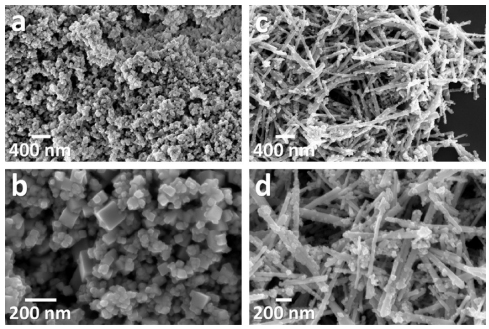

Figure 2. FESEM images (secondary electrons) of ceria nanocubes (a,b) and ceria nanorods (c,d) after drying.

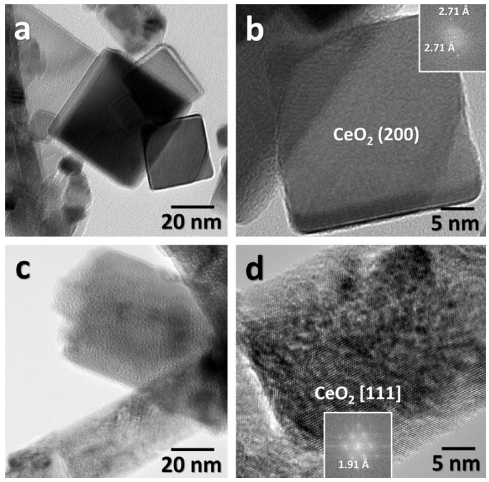

Figure 3. HRTEM images of fresh ceria nanocubes (a,b) and ceria nanorods (c,d).

direction within a nanorod with the corresponding FT image showing spots at 1.91 Å of (220) planes of ceria. A higher degree of surface irregularities, such as defects and surface roughness, is observed on nanorods, in agreement with recent reports.[15,35]

According to the literature, morphological changes are expected to occur above 773 K, and Figure 4 shows FESEM

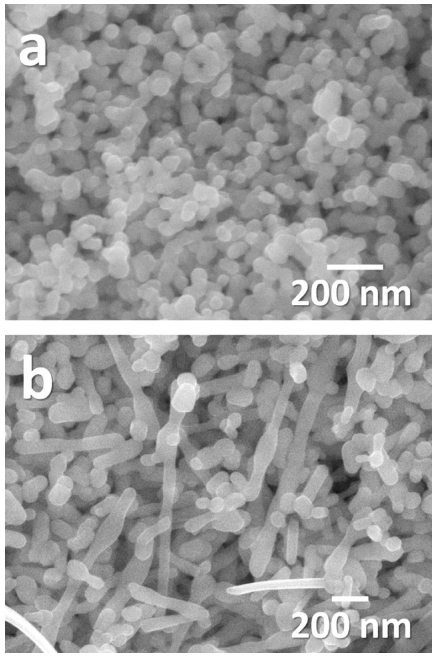

Figure 4. FESEM images (secondary electrons) of aged ceria nanocubes (a) and ceria nanorods (b).

characterization of nanocubes and nanorods subjected to aging under air at 1023 K for 4 h. Ceria nanocubes (Figure 4a) do not exhibit sharp edges after the aging treatment. A careful examination by HRTEM (Figure 5) indicates that the sample consists of ceria nanocubes with capped edges. Most particles measure between 20 and 50 nm in size, and there are abundant junctions between them that are readily seen in the low magnification TEM image shown in Figure 5a. Figure 5 b–d corresponds to HRTEM images of individual particles. In Figure 5b lattice fringes at 2.71 Å, which are ascribed to the (200) planes of CeO_2, correspond to a nanocube oriented along the [100] crystallographic direction; however, and in

dx.doi.org/10.1021/cs400850r | ACS Catal. 2014, 4, 172–181

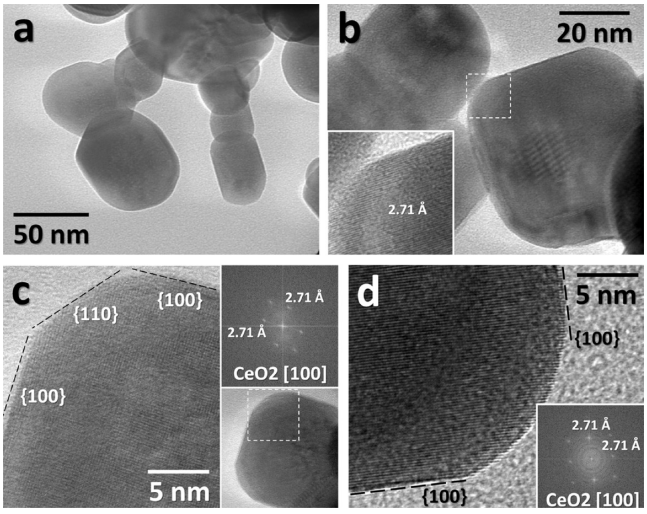

Figure 5. HRTEM images of aged ceria nanocubes.

contrast to the sample before aging, capped edges are easily recognized. A nice HRTEM image is depicted in Figure 5c, where a truncated nanocube is oriented along the [100] direction and shows {100} planes at 90° (see the Fourier transform image in the inset). In addition to the {100}-type edges of the crystallite, additional and well-defined edges corresponding to {110}-type planes are also clearly seen at 45°. These new {110} planes originate from the truncation of the original edges and are somehow curved, thus implying the existence of other planes with higher Miller indexes, which might be very reactive.

Another clear example of such edge truncation is shown in Figure 5d. Again, there is a change of geometry from cubic to truncated cubic (and sometimes nearly spherical ceria particles) upon thermal treatment. The morphology evolution of ceria nanocubes upon thermal treatment has not been investigated in detail; it is reported that the shapes of the nanocubes are well kept at temperatures below 773 K, and only at higher temperatures are morphological modifications evident in the TEM meaurements[36] with observation of "rounded" particles. We have also observed nearly rounded particles after aging at 1023 K (see Figures 4a and 5a); these particles likely originate by progressive modification of a cubic geometrical shape to a cube with all corners truncated as a first step, followed by formation of cubes with edges and corners truncated, and finally, an irregular truncated cube-octahedron, which would result in HRTEM images as a quasi rounded particle.[45] This evolution can be depicted as in Figure 6 and is in agreement with the development of geometries obtained by high-temperature simulated amorphization and recrystallization of ceria cubes.[46]

A nanorod sample consists of ceria rods with various thicknesses and lengths. Clearly, the original ceria nanorods have suffered during the treatment, and they do not exhibit regular and parallel cylindrical shapes, as shown by FESEM in Figure 4b. Their heterogeneous aspect is clearly seen in the low-magnification TEM image shown in Figure 7a. Interest-

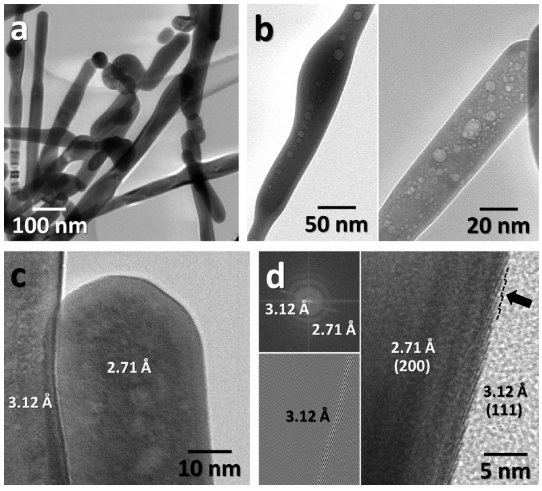

Figure 7. HRTEM images of aged ceria nanorods.

ingly, the rods contain abundant voids/porosity from few nanometers up to 10 nm in size. These pores, which are characterized by a spherical shape, were not present before the treatment and appear brighter in the TEM image as a result of lower electron contrast, as clearly observed in Figure 7b. The drop we observed in surface area following thermal treatment of the nanorods indicates that the formation of this pore network is difficult to access from the outside and does not influence specific surface. A similar porosity network has been recently observed in ceria nanorods, although a definite answer regarding their characteristics has not yet been given.[47] The rods are completely crystalline, as seen in the HRTEM image depicted in Figure 7c. Lattice fringes at 2.71 and 3.12 Å correspond to (200) and (111) crystallographic planes of ceria, respectively; however, distorted surfaces are observed in some rods. In the HRTEM image shown in Figure 7d, two different lattice fringes are recognized in a single rod, which bring about strips in the Fourier transform image (see inset). A filtered image obtained by selecting the portion of the strip corresponding to 3.12 Å is included. By doing so, a brighter portion is obtained, which corresponds exactly to the surface of the rod. Therefore, the rod is aligned along (200) planes, but at the surface, there is a layer of about 1−2 nm thick with (111) planes. In addition, these surface (111) planes are arranged in steps, as shown in the figure (see arrow). These steps, together

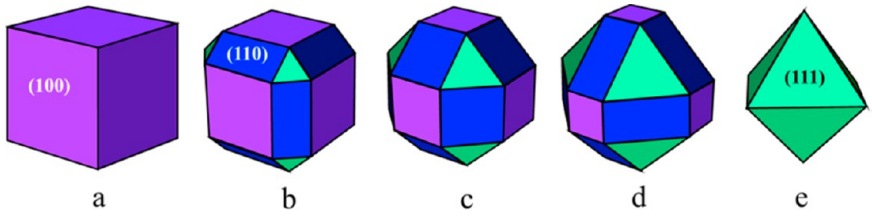

Figure 6. Transition of cubic (a) and octahedral particles (e) into edge- and corner-truncated cubes and octahedra (b, c, d) for effect of thermal treatment.

dx.doi.org/10.1021/cs400850r | ACS Catal. 2014, 4, 172−181

with the occurrence of such narrow surface rearrangement, may bring about a very reactive surface.

We have reported the HRTEM of conventional ceria polycrystalline powders in previous investigations.[32,33] By identifying the lattice spacings and particle orientation, the facets on the particle surfaces were determined, and it was found that in samples treated at low temperatures (below 973 K), the dominant lattice fringes in all cases correspond to the {111} family, and only a few {100} facets are found. This is compatible with the shape of most particles defined by {111} plane-enclosed octahedrons, indicating fast growth along the [111] direction and a minority of particles dominated by truncated octahedron defined by {100} and {111} facets, in agreement with other studies.[4,45] After calcination, a higher ratio of reactive {100} facets are generated that are attributed to the favorable formation of an irregular metastable truncated octahedral structure by aggregation of smaller CeO_2 crystals upon annealing.

3.2. Thermal, Reduction, and Redox Behavior of Ceria Nanoparticles. Thermogravimetry profiles of the three series of samples are shown in Figure 8. Nanocubes show a 1% weight

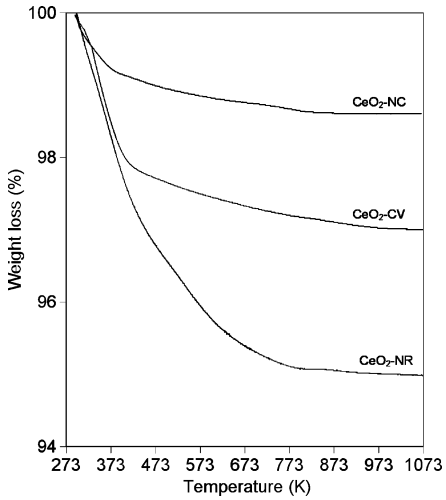

Figure 8. TGA profiles under air flow of polycrystalline and nanoshaped ceria.

loss, mainly concentrated in the low temperature region (T < 450 K), indicating the presence of a negligible amount of adsorbed water. Nanorods show ~5% weight loss in the range of temperature 373−773 K, which can be attributed to removal of molecular water and dehydration of precipitate, residual cerium chloride/hydroxychloride decomposition, or both.[48−50] An intermediate behavior is observed with conventional ceria powders that show a loss of 2.5 wt %. No indication of carbonate decomposition was found in this temperature range, as evidenced by coupled TG−MS analysis.

The reduction of surface and bulk ceria crystals was studied by hydrogen temperature-programmed reduction. It is known that TPR of ceria gives indications on reducibility of surface and bulk cerium ions; reduction of conventional CeO_2 powders is characterized by a bimodal shape with a low temperature peak characteristic of surface reduction and a large peak at high temperature typical of bulk oxide reduction.[51] The TPR of samples investigated here are reported in Figure 9. Reduction of fresh CeO_2-CV shows two major peaks at ~500 and 800 °C attributed to surface and bulk reduction. After aging, a

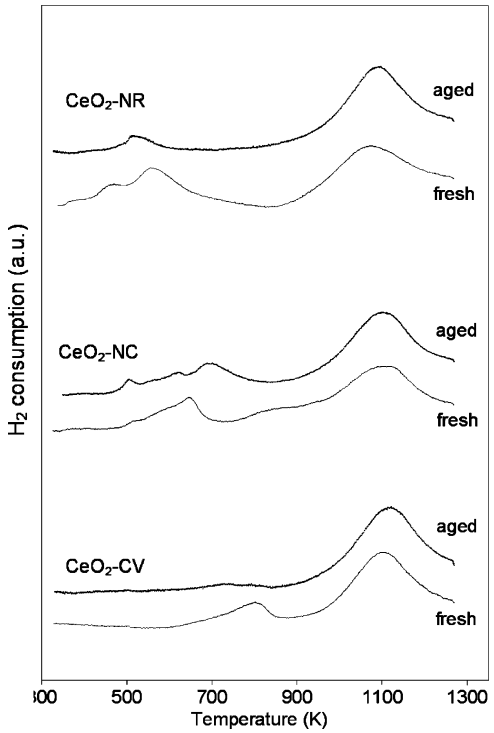

Figure 9. H_2-TPR profiles of fresh and aged samples.

reduction of intensity of the low-temperature peak is observed, in agreement with the drop in surface area. A decrease in the surface reduction temperature by more than 100° and 200° is observed with nanocubes and nanorods, respectively. In addition, hydrogen consumption at low temperature is higher in nanoshaped samples compared wiht conventional ceria powders, indicating that lattice oxygen can be involved in reduction at lower temperature in these samples, at least for the smaller ceria crystals. After aging, a temperature shift and a decrease in intensity of the surface reduction peak is observed in both samples, in agreement with the surface area drop; this is accompanied by an increase in the intensity of the bulk reduction peak. Overall reduction degree, calculated by integrating TPR profiles (Table 1), shows that a higher degree of reduction is obtained with nanoshaped samples both in fresh state and after aging. The reduction behavior is in agreement with the oxygen storage capacity measured at 673 K (Table 1). Nanoshaped samples have a higher OSC compared with conventional ceria powders; in addition, the measured OSC of ceria nanocubes and nanorods are higher than those calculated according to the theoretical OSC of {100}, {110}, and {111} surfaces,[18,52] indicating that OSC at 673 K takes place also in the bulk for these samples. Oxygen storage behavior is not influenced by treatment under redox conditions, as reported in Table 2, which shows OSC values after three reduction/oxidation cycles at 673 K. No associated changes in the morphology of the nanostructures are observed following OSC cycles.

3.3. Soot Oxidation Activity. A representative weight-loss curve showing the effect of different ceria particles on soot oxidation profile under TG conditions (tight contact) is reported in Figure 10 for CeO_2-CV, -NC, and -NR samples, respectively, in the fresh state and after thermal aging. Soot oxidation starts in the range of 600−650 K and is completed at a temperature of ~780−800 K for the less active samples. The

dx.doi.org/10.1021/cs400850r | ACS Catal. 2014, 4, 172−181

Table 2. OSC Data after Repeated Reduction/Oxidation Cycles

sample	OSC (μmol O/m^2)		
	1st cycle	2nd cycle	3rd cycle
CeO_2-NC_f	6.1	7.8	7.8
CeO_2-NC_a	11.2	12.3	12.3
CeO_2-NR_f	6.3	6.3	7.2
CeO_2-NR_a	9.9	10.4	10.4

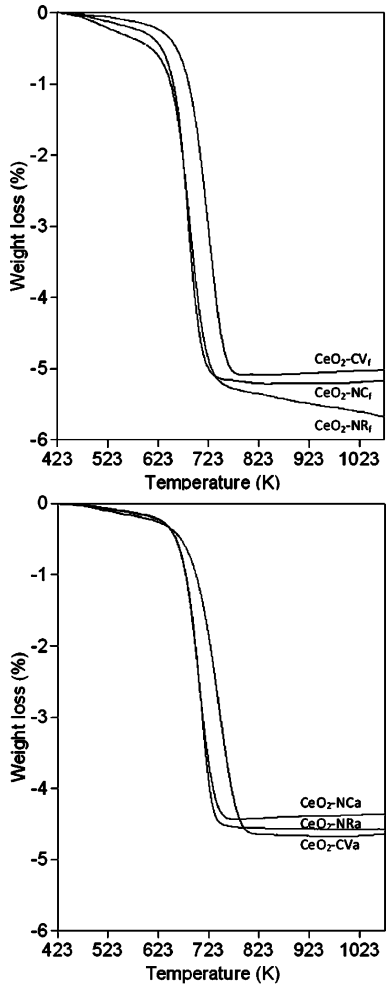

Figure 10. Weight-loss profile of soot-catalyst mixture under tight contact conditions.

T_{50} values are reported in Figure 11; under tight contact conditions, T_{50} values for fresh samples range between ~680 and 720 K. Nanoshaped materials are more active than conventional ceria sample of equivalent surface area, as shown by the lower T_{50}. The activity of these samples compares favorably also with the activity of conventional high-surface-area ceria, which shows a T_{50} only a few degrees lower than that of fresh nanocubes and nanorods. An increase in the T_{50} is observed after aging as a result of the drop in surface area for all the samples, in agreement with that found in the literature when overall activity is monitored under tight contact conditions.[53] Overall the activity compared for samples in the same surface area range increases using nanoshaped ceria, as shown by the decrease in the T_{50} of ~30 K. A similar behavior is reported when measuring activity under loose conditions. In this case, T_{50} for nanoshaped materials is ~60 K lower than for conventional ceria.

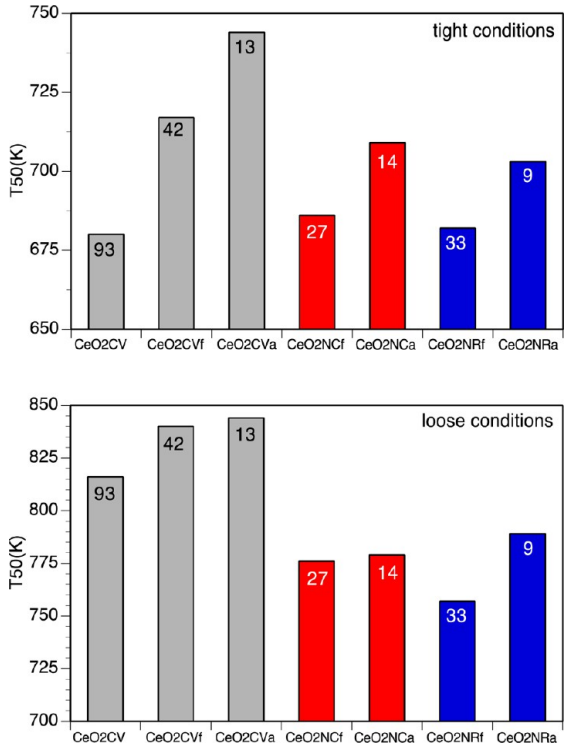

Figure 11. Soot combustion activity (as T_{50}) of fresh and aged samples under tight and loose conditions. Surface area values are indicated in the bars.

For all samples, in addition to the T_{50}, quantitative measurements of the specific activity under isothermal conditions was also carried out according to the method described in the Experimental section considering the effect of BET surface area. Table 3 shows rate data per BET surface area and on a per gram basis measured at a reference temperature of 673 and 773 K for all ceria samples under tight and loose conditions. In contrast to temperature-programmed measurements, for which activity decreases with aging, the specific rate on a surface area basis is shown to increase against calcination temperature for all samples, regardless of soot−catalyst mixing conditions. Under tight mixing mode, the rise of activity is larger for conventional ceria and less significant for nanorods and nanocubes, whereas under loose conditions, the change of activity is relevant for all samples.

Table 3. Rate Data for Soot Oxidation Reaction

sample	$rate_{tight}$ [a]	$rate_{tight}$ [b]	activation energy[c]	$rate_{loose}$ [a]	$rate_{loose}$ [b]
CeO_2-CV	465	5	58	279	3
CeO_2-CV_f	504	12	66	420	10
CeO_2-CV_a	221	17	71	377	29
CeO_2-NC_f	405	15	70	702	26
CeO_2-NC_a	308	22	78	700	50
CeO_2-NR_f	561	17	69	429	13
CeO_2-NR_a	171	19	76	279	31

[a]Value in $\mu g_{soot} \cdot g_{soot\_initial} \cdot s^{-1} \cdot g^{-1}$ (× 100), measured at 673 K for tight and at 773 K for loose contact conditions. [b]Value in $\mu g_{soot} \cdot g_{soot\_initial} \cdot s^{-1} \cdot m^{-2}$ (× 100), measured at 673 K for tight and at 773 K for loose contact conditions. [c]Measured under tight conditions (kJ/mol).

dx.doi.org/10.1021/cs400850r | ACS Catal. 2014, 4, 172−181

The activation energies for reaction under tight conditions are reported in Table 3. The values are in the range 58−80 kJ/mol and are in line with measurements made on the same reaction carried out over ceria-based materials.[54] The nanocubes and nanorods are characterized by slightly higher values of activation energies under fresh conditions compared with conventional material. Aging is shown to increase activation energies with all catalyst compositions; higher activation energies can therefore be associated with reaction over more active surfaces.

4. DISCUSSION

The catalytic properties of cerium oxide are strongly affected by the type and nature of exposed surfaces. The recent advances in the preparation of nanoshaped cerias enabled the study of the correlation between exposed surfaces (more commonly belonging to the {111}, {110} and {100} families) and activity in several important reactions. It is clearly established that in these materials, the exposure of less stable {100}- and {110}-type surfaces positively affects the catalytic activity in carbon monoxide oxidation,[7] and the same surfaces promote ceria reduction by either hydrogen or carbon monoxide.[35] We have also recently shown that high-temperature treatment of conventional polycrystalline ceria powder, which exposes preferentially the {111}-type surfaces, induces a surface rearrangement toward the formation of more reactive surface planes belonging to the {100} and {110} families associated with a decrease of exposure of the less reactive {111} facets. As a consequence, aging of polycrystalline ceria resulted in higher specific rates of CO oxidation, although the overall conversion decreased due to the reduction in specific surface area induced by thermal treatment.[32] We have shown that the same behavior can be observed when soot oxidation is carried out over ceria and ceria−zirconia;[33] also in this case, the increase in the specific rate of soot oxidation originating from exposure of more reactive surfaces cannot compensate for a loss in the surface area caused by thermal treatment, and the overall activity measured as T_{50} decreased.

The results presented here show clear evidence of the effect of surface exposure in the reactivity of ceria for soot oxidation reaction by comparing the reactivity in terms of T_{50} and the reaction rate of both conventional and nanoshaped materials. For ceria nanocubes and nanorods, the experimental T_{50} values were comparable and nearly 30 K lower than those of conventional samples with a similar surface area; this indicates a higher activity and was confirmed by direct rate measurements reported in Table 2. By considering that the as-prepared conventional ceria powders mainly consist of particles enclosed by eight {111}-type planes, whereas nanorods and nanocubes crystals are enclosed within a mixture of {110}/{100}/{111} and {100} planes, respectively, we can suggest that {100}/{110} exposed surfaces are more reactive in soot oxidation. From the comparison of the reactivity data, we cannot distinguish if one of the surface types is more active. Data reported in the literature for other reactions indicate that the order of reactivity is nanocubes > nanorods > polycrystalline ceria, which is the reverse order of their main surface stability; that is, {100} < {110} < {111}.[55]

Aging of all samples resulted in more active catalysts, as shown by looking at the reaction rate against calcination temperatures. The increase in the specific reaction rate can be associated with the morphological changes occurring in conventional and nanoshaped samples after aging. As evidenced by HRTEM, these modifications increase the number of exposed {100} and {110} planes in conventional ceria crystals through the formation of a truncated octahedron geometry (from e to d in Figure 6) and promote the appearance of {110} facets and additional surface corners and edges in nanocubes by an edge-/corner-truncation process (from a to b in Figure 6). As a result, after thermal aging, similar particle shape/morphology (b, c, and d in Figure 6) develops starting from either cubes or octahedral particles. The overall activity of aged samples will depend on the distribution of these particles and on the nature of exposed surfaces. Therefore, regardless of the initial geometry (conventional/octahedral particles vs nanoshaped/cubic particles), we end up with particle shapes that have a quite similar specific activity and comparable values of activation energies; this links the reactivity of the octahedral particles in conventional ceria powders with that of the cubes in the nanoshaped materials. With nanorods, surface rearrangements during heat treatment may promote the location of oxygen on steps, edges, and corners, which is normally more reactive than oxygen located on flat surfaces.[21] When measuring TG profiles, the increase in the specific activity after calcination is masked by the drop in the surface area, as indicated by the value of T_{50}, which increases following thermal aging; only isothermal reaction rate measurements normalized per BET surface area allow quantification of the difference in activity.

The most accepted mechanism for soot oxidation over ceria relies on its reduction by carbon soot at the ceria/soot contact points to promote formation of active oxygen species, such as superoxide (O_2^-), via oxygen adsorption on the reduced surface of ceria in the vicinity of soot according to[27]

$$Ce^{3+}-\square + O_2 \rightarrow Ce^{4+}-(O_2)^-$$

Under these conditions, reduced ceria would be the starting point for the formation of the active superoxide ion, which then reacts with carbon to form CO_2. Ceria can be reduced by soot in the contact points located at the soot/ceria interface, and this will initiate the "active oxygen" path, which would contribute to the direct oxidation of soot particles by a spillover mechanism. It is therefore clear that reduction of ceria and consequent vacancy formation is an important step in the overall soot oxidation process. We have already shown that the step of vacancy formation operated by carbon is strongly dependent on the type of planes exposed, being facilitated over the {110} family as compared with the {111} type.[33]

We have also shown that both TPR and OSC evidence that surfaces of cubes and rods are reduced by hydrogen more easily than conventional ceria. In addition, OSC reveals that the associated migration of lattice oxygen from the bulk to the surface is much easier in {100}- and {110}-type surfaces. Similar results were found by Wang et al.[19] and Mai et al.,[18] who reported an increase in OSC when measured in nanoshaped cerias due to the participation of bulk oxygen and by Desaunay et al.,[35] who reported the order of reactivity in TPR for surface reduction in agreement with {100} > {110} > {111}. Previous computer modeling showed that the {111}-type surface is the most stable, with the lowest surface energy followed by the {110} and, finally, by the more energetic {100}, {210}, and {310},[56,57] which are believed to be the most reactive. Because the mechanism of soot oxidation leads to the formation of an oxygen vacancy, the formation energy of a surface oxygen vacancy is likely to play an important role in the enhancement of activity. Recent DFT calculations indicate that

dx.doi.org/10.1021/cs400850r | ACS Catal. 2014, 4, 172−181

the formation energies of ceria surface oxygen vacancies are the lowest in {110}, followed by {100} and {111},[58] which is also in agreement with the increase in activity in nanoshaped materials as compared with conventional ceria powders.

5. CONCLUSIONS

In summary, we have shown that carbon soot oxidation activity is dependent on the shape of the ceria nanoparticles, and in addition to the exposed surface, the activity is largely influenced by the surface area. By comparing samples within the same surface area range, higher activity and conversion is observed over nanocubes and nanorods as compared with polycrystalline ceria octahedral particles. Thermal aging at $T > 773$ K markedly affects the crystal shape by truncation of the edges and corners, generating surfaces with higher index plane exposure. This changes the number and type of planes exposed, resulting in an increase in the specific activity, which is more relevant in polycrystalline ceria than in cubes and rods. The increase in the specific activity is accompanied by a decrease in the surface area that negatively affects the overall conversion. Interestingly, it is shown that starting either from nanocubes or from polycrystalline ceria, similar morphologies and shapes are obtained after aging. These results open up new possibilities in the design of highly active ceria-based catalysts with controlled morphologies.

AUTHOR INFORMATION

Corresponding Author

*E-mail: trovarelli@uniud.it.

Notes

The authors declare no competing financial interest.

ACKNOWLEDGMENTS

We are grateful to Regione Friuli Venezia Giulia for support in part through LR 14/2010. We also are thankful for financial support from Italy–Austria Interreg IV project Mat4Cata. E.A. is thankful for financial support from MIUR (Futuro in ricerca, project SOLYST). J.L. is grateful to the ICREA Academia program and to the MINECO project ENE2012-36368.

REFERENCES

(1) Zhou, K.; Li, Y. *Angew. Chem., Int. Ed.* **2012**, *51* (3), 602–13.
(2) Yuan, Q.; Duan, H. H.; Li, L. L.; Sun, L. D.; Zhang, Y. W.; Yan, C. H. *J. Colloid Interface Sci.* **2009**, *335* (2), 151–167.
(3) Trovarelli, A.; Fornasiero, P. In *Catalysis by Ceria and Related Materials*, 2nd ed.; Imperial College Press: London, 2013; p 888.
(4) Wang, Z. L.; Feng, X. D. *J. Phys. Chem. B* **2003**, *107* (49), 13563–13566.
(5) Zhou, K. B.; Wang, X.; Sun, X. M.; Peng, Q.; Li, Y. D. *J. Catal.* **2005**, *229* (1), 206–212.
(6) Pan, C. S.; Zhang, D. S.; Shi, L. Y.; Fang, J. H. *Eur. J. Inorg. Chem.* **2008**, *15*, 2429–2436.
(7) Wu, Z. L.; Li, M. J.; Overbury, S. H. *J. Catal.* **2012**, *285* (1), 61–73.
(8) Renuka, N. K.; Praveen, A. K.; Aniz, C. U. *Microporous Mesoporous Mater.* **2013**, *169*, 35–41.
(9) Li, J. F.; Lu, G. Z.; Li, H. F.; Wang, Y. Q.; Guo, Y.; Guo, Y. L. *J. Colloid Interface Sci.* **2011**, *360* (1), 93–99.
(10) Tana; Zhang, M. L.; Li, J.; Li, H. J.; Li, Y.; Shen, W. J. *Catal. Today* **2009**, *148* (1–2), 179–183.
(11) Du, X.; Zhang, D.; Shi, L.; Gao, R.; Zhang, J. *J. Phys. Chem. C* **2012**, *116* (18), 10009–10016.
(12) Hsiao, W. I.; Lin, Y. S.; Chen, Y. C.; Lee, C. S. *Chem. Phys. Lett.* **2007**, *441* (4–6), 294–299.
(13) Chowdhury, S.; Lin, K.-S. *J. Nanomater.* **2011**, *2011*, 1–16.
(14) Han, W. Q.; Wen, W.; Hanson, J. C.; Teng, X. W.; Marinkovic, N.; Rodriguez, J. A. *J. Phys. Chem. C* **2009**, *113* (52), 21949–21955.
(15) Agarwal, S.; Lefferts, L.; Mojet, B. L.; Ligthart, D. A. J. M.; Hensen, E. J. M.; Mitchell, D. R. G.; Erasmus, W. J.; Anderson, B. G.; Olivier, E. J.; Neethling, J. H.; Datye, A. K. *ChemSusChem* **2013**, *6*, 1898–1906.
(16) Ta, N.; Liu, J.; Chenna, S.; Crozier, P. A.; Li, Y.; Chen, A.; Shen, W. *J. Am. Chem. Soc.* **2012**, *134*, 20585–20588.
(17) Mullins, D. R.; Albrecht, P. M.; Calaza, F. *Top. Catal.* **2013**, *56*, 1345–1362.
(18) Mai, H. X.; Sun, L. D.; Zhang, Y. W.; Si, R.; Feng, W.; Zhang, H. P.; Liu, H. C.; Yan, C. H. *J. Phys. Chem. B* **2005**, *109* (51), 24380–24385.
(19) Wang, D. Y.; Kang, Y. J.; Doan-Nguyen, V.; Chen, J.; Kungas, R.; Wieder, N. L.; Bakhmutsky, K.; Gorte, R. J.; Murray, C. B. *Angew. Chem., Int. Ed.* **2011**, *50* (19), 4378–4381.
(20) Zhang, J.; Kumagai, H.; Yamamura, K.; Ohara, S.; Takami, S.; Morikawa, A.; Shinjoh, H.; Kaneko, K.; Adschiri, T.; Suda, A. *Nano Lett.* **2011**, *11* (2), 361–4.
(21) Sayle, T. X. T.; Cantoni, M.; Bhatta, U. M.; Parker, S. C.; Hall, S. R.; Mobus, G.; Molinari, M.; Reid, D.; Seal, S.; Sayle, D. C. *Chem. Mater.* **2012**, *24* (10), 1811–1821.
(22) Nolan, M.; Grigoleit, S.; Sayle, D. C.; Parker, S. C.; Watson, G. W. *Surf. Sci.* **2005**, *576* (1–3), 217–229.
(23) Bueno-López, A. *Appl. Catal., B* **2014**, *146*, 1–11.
(24) Aneggi, E.; Boaro, M.; de Leitenburg, C.; Dolcetti, G.; Trovarelli, A. *J. Alloys Compd.* **2006**, *408*, 1096–1102.
(25) Atribak, I.; Lopez-Suarez, F. E.; Bueno-Lopez, A.; Garcia-Garcia, A. *Catal. Today* **2011**, *176* (1), 404–408.
(26) Issa, M.; Petit, C.; Brillard, A.; Brilhac, J.-F. *Fuel* **2008**, *87* (6), 740–750.
(27) Machida, M.; Murata, Y.; Kishikawa, K.; Zhang, D.; Ikeue, K. *Chem. Mater.* **2008**, *20* (13), 4489–4494.
(28) Bassou, B.; Guilhaume, N.; Iojoiu, E. E.; Farrusseng, D.; Lombaert, K.; Bianchi, D.; Mirodatos, C. *Catal. Today* **2011**, *159* (1), 138–143.
(29) Reddy, B. M.; Bharali, P.; Thrimurthulu, G.; Saikia, P.; Katta, L.; Park, S.-E. *Catal. Lett.* **2008**, *123* (3–4), 327–333.
(30) Aneggi, E.; de Leitenburg, C.; Trovarelli, A. *Catal. Today* **2012**, *181* (1), 108–115.
(31) Krishna, K.; Bueno-Lopez, A.; Makkee, M.; Moulijn, J. A. *Top. Catal.* **2007**, *42–43* (1–4), 221–228.
(32) Aneggi, E.; Llorca, J.; Boaro, M.; Trovarelli, A. *J. Catal.* **2005**, *234* (1), 88–95.
(33) Aneggi, E.; de Leitenburg, C.; Llorca, J.; Trovarelli, A. *Catal. Today* **2012**, *197* (1), 119–126.
(34) Wu, Q.; Zhang, F.; Xiao, P.; Tao, H. S.; Wang, X. Z.; Hu, Z.; Lu, Y. N. *J. Phys. Chem. C* **2008**, *112* (44), 17076–17080.
(35) Désaunay, T.; Bonura, G.; Chiodo, V.; Freni, S.; Couzinié, J. P.; Bourgon, J.; Ringuedé, A.; Labat, F.; Adamo, C.; Cassir, M. *J. Catal.* **2013**, *297*, 193–201.
(36) Wu, Z. L.; Li, M. J.; Howe, J.; Meyer, H. M.; Overbury, S. H. *Langmuir* **2010**, *26* (21), 16595–16606.
(37) Jenkins, E.; Snyder, R. In *Introduction to Powder X-ray Diffractometry*; Wiley: New York, 1996.
(38) Toby, B. H. *J. Appl. Crystallogr.* **2001**, *34*, 210–213.
(39) Larson, A. C.; Dreele, R. B. V. *General Structure Analysis System "GSAS"*; Los Alamos National Laboratory: Los Alamos, NM, 2000.
(40) Mamontov, E.; Brezny, R.; Koranne, M.; Egami, T. *J. Phys. Chem. B* **2003**, *107* (47), 13007–13014.
(41) Jelles, S. J.; van Setten, B.; Makkee, M.; Moulijn, J. A. *Appl. Catal., B* **1999**, *21* (1), 35–49.
(42) Maensiri, S.; Masingboon, C.; Laokul, P.; Jareonboon, W.; Promarak, V.; Anderson, P. L.; Seraphin, S. *Cryst. Growth Des.* **2007**, *7* (5), 950–955.
(43) Chowdhury, S.; Lin, K.-S. *Mater. Chem. Phys.* **2012**, *133* (1), 163–169.

(44) Tao, Y.; Gong, F. H.; Wang, H.; Wu, H. P.; Tao, G. L. *Mater. Chem. Phys.* **2008**, *112* (3), 973−976.
(45) Tan, J. P. Y.; Tan, H. R.; Boothroyd, C.; Foo, Y. L.; He, C. B.; Lin, M. *J. Phys. Chem. C* **2011**, *115* (9), 3544−3551.
(46) Sayle, T. X. T.; Parker, S. C.; Sayle, D. C. *Chem. Commun.* **2004**, *21*, 2438−2439.
(47) Florea, I.; Feral-Martin, C.; Majimel, J.; Ihiawakrim, D.; Hirlimann, C.; Ersen, O. *Cryst. Growth Des.* **2013**, *13* (3), 1110−1121.
(48) Hassanzadeh-Tabrizi, S. A.; Taheri-Nassaj, E. *Ceram. Int.* **2011**, *37* (4), 1251−1257.
(49) Hosokawa, S.; Iwamoto, S.; Inoue, M. *J. Alloys Compd.* **2006**, *408*, 529−532.
(50) Zehnder, R. A.; Clark, D. L.; Scott, B. L.; Donohoe, R. J.; Palmer, P. D.; Runde, W. H.; Hobart, D. E. *Inorg. Chem.* **2010**, *49* (11), 4781−90.
(51) Giordano, F.; Trovarelli, A.; de Leitenburg, C.; Giona, M. *J. Catal.* **2000**, *193* (2), 273−282.
(52) Madier, Y.; Descorme, C.; Le Govic, A. M.; Duprez, D. *J. Phys. Chem. B* **1999**, *103* (50), 10999−11006.
(53) Krishna, K.; Bueno-Lopez, A.; Makkee, M.; Moulijn, J. A. *Appl. Catal., B* **2007**, *75* (3−4), 210−220.
(54) Bokova, M. N.; Decarne, C.; Abi-Aad, E.; Pryakhin, A. N.; Lunin, V. V.; Aboukais, A. *Thermochim. Acta* **2005**, *428*, 165−171.
(55) Yang, Z. X.; Woo, T. K.; Baudin, M.; Hermansson, K. *J. Chem. Phys.* **2004**, *120* (16), 7741−7749.
(56) Sayle, T. X. T.; Parker, S. C.; Catlow, C. R. A. *Surf. Sci.* **1994**, *316* (3), 329−336.
(57) Conesa, J. C. *Surf. Sci.* **1995**, *339* (3), 337−352.
(58) Nolan, M.; Parker, S. C.; Watson, G. W. *Surf. Sci.* **2005**, *595* (1−3), 223−232.